X-ray diffraction and X-ray absorption of strained CoO and MnO thin films

Csiszár, Szilárd Istvan; Tjeng, L.H

Chapter 4

Probing the electronic and magnetic structure of transition-metal oxide thin films

4.1 Introduction

The use of synchrotron radiation based high energy spectroscopies such as linearly and circularly polarized soft-x-ray absorption spectroscopy is relatively new [1]. This type of spectroscopy has been developed into full maturity only in the last 15 years, both in terms of instrumentation as well as in terms of a quantitative theoretical analysis of the spectra, which are often dominated by multiplet structures [2–4]. In fact, it all started with the pioneering work of Fink, Thole, Sawatzky and Fuggle, who used high energy electron-energy-loss spectroscopy to study narrow band and impurity systems, and recognized that the observed multiplet structures can provide an extremely detailed information about the local electronic structure of systems involving transition-metal and rare-earth atoms [5–8]. The underlying principle is the fact that the core hole produced has a strong attractive Coulomb interaction with the valence electrons. For strongly correlated oxides, this interaction is much larger than the one-electron band width of the valence electrons. The absorption process is therefore strongly excitonic and the spectra can then be understood in a straightforward manner in terms of atomic-like transitions.

These spectra are not only element specific, but above all, their multiplet structures are extremely sensitive to the charge, spin and orbital state of the ion due to the very effective dipole selection rules associated with the K ($1s \rightarrow 2p$), $L_{2,3}$ ($2p \rightarrow 3d$), and $M_{4,5}$ ($3d \rightarrow 4f$) transitions for the oxygen,

transition metal and rare-earth ions, respectively. In fact, the specificity to the initial state symmetry is so large, that one does not need a very good energy resolution in order to measure which of the possible initial state symmetries is occupied, since different symmetries lead to completely different multiplet structured spectra. In other words, an experimental energy resolution of 500 meV is often enough to distinguish initial states that are different by not more than a few meV or less in energy, making the technique extremely valuable for the study of electronic and magnetic phase transitions which usually occur in the temperature range up to roughly room temperature (kT_c = 25 meV). This is clearly demonstrated in later experiments using synchrotron radiation in the soft-x-ray region [2, 9–30].

Very important in this context was the development of sum rules, by which the separate orbital and spin contributions to the total magnetic moment in ferromagnetic materials can be deduced directly from the integrated circularly-polarized x-ray absorption spectra, without having to rely on simulations of the spectra [31–33]. This provides a considerable simplification for the use of the technique for the study of (multi-element) magnetic materials.

In addition, soft X-ray absorption spectroscopy is a surface sensitive technique. This aspect makes it extremely suitable to characterize the chemical composition, magnetic properties and electronic structure of surfaces, thin films and multilayers. In fact, there are not many spectroscopic tools that have the sensitivity to deal with such minute amounts of material.

Finally, it is worthwhile to mention that soft-x-ray absorption spectroscopy may be the only technique that has sufficient contrast for the orbital symmetry of the electrons, yielding information that is crucial to unravel the interplay between spin and orbital degrees of freedom in correlated oxides. This is a necessity for the understanding of, for instance, the magnetic properties of transition metal oxides with a high magnetocrystalline anisotropy.

4.2 Synchrotron radiation

First observed as an energy loss in electron storage rings, synchrotron radiation turned out to be a very useful source of electromagnetic radiation. Synchrotrons originally developed for the study of elementary particles are nowadays mostly used as powerful photon sources. These facilities are capable of generating electromagnetic radiation ranging from infra-red to hard X-rays. The principle is based on the radiation of electromagnetic waves from charged particles (electrons) undergoing an accelerated motion when passing through a magnetic field. Three types of magnet structures that are commonly used to generate synchrotron radiation are: bending magnets, undulators and wigglers. For more details about the synchrotron radiation we refer the reader to [34, 35].

Our soft X-ray absorption measurements were carried out at National Synchrotron Radiation Research Center (NSRRC) Taiwan. The beamline used for this purpose was the original Dragon beamline built by C.T. Chen and F. Sette at the National Synchrotron Light Source, Brookhaven National Laboratory and later moved to Taiwan. It delivers soft X-rays from a bending magnet in an energy range of 90-1200 eV [36–38]. This beamline and the NSRRC storage ring fulfilled completely the needs of our experiment which were a high degree of linear polarization, extreme intensity and energy stability as well as high resolution. Figure 4.1 sketches the layout of the Dragon monochromator.

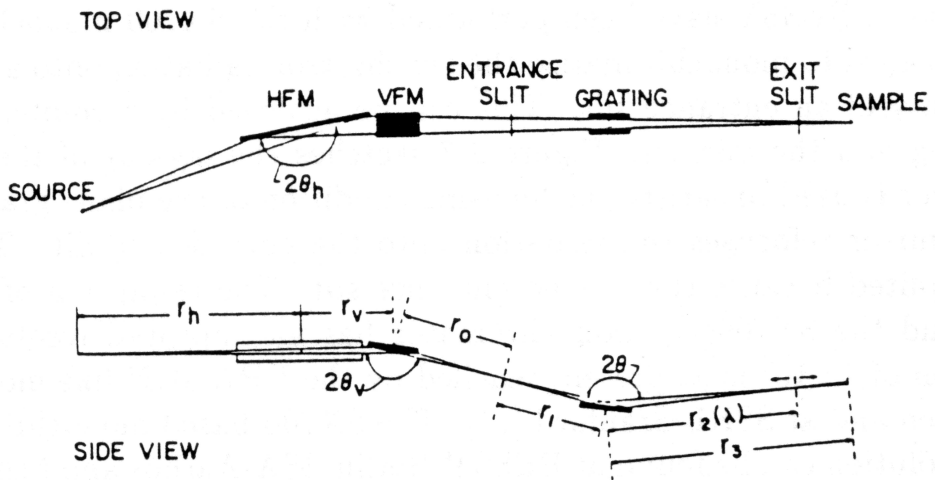

Figure 4.1: Dragon monochromator taken from ref [38].

The idea of designing a monochromator with a simple arrangement of spherical optical elements [36] turned out to be a great success, achieving an unprecedented high resolution of $1{:}10^4$ in the soft X-ray range. The horizontal and vertical focusing mirrors (HFM and VFM), which direct the radiation from the bending magnet and to allow the selection of linear or circular polarized light are followed by the entrance slit. This slit improves the resolution by making the monochromator less dependent on the source size. The grating which diffracts and focuses the photon beam is followed by a movable exit slit in order to follow the focus at different wavelengths. The overall photon energy resolution was usually set to 0.3∼0.4 eV for photon energies between 600-800 eV.

4.3 Principles of soft X-ray absorption

The absorption of X-rays arises as a result of a photoelectron process, which transfers an electron from a core level (1s, 2s, 2p) to the empty valence levels above the Fermi level. This is exemplified in Figure 4.2(a) where we use a one electron picture to describe the process. Later we will show that this picture is actually quite incorrect due to strong electron-electron correlation effects. The detection of the absorption process can be done in many ways. These possibilities are depicted in Figure 4.3. The most straight-forward method one can think of, is by measuring the number of incident photons and the number of transmitted photons trough a thin foil, this method is the so-called *transmission mode*. The ratio between the two numbers will be an exponential function of the absorption coefficient. Although this measurement method would be intuitively the most reliable one, the realization of the actual measurement is quite a challenge. The reason for this is that soft X-rays are strongly absorbed by matter. Just to give an example the absorption of X-rays for Ni is almost two orders of magnitude higher at 1 keV than at 8 keV photon energy (see for example ref. [39]). Therefore, in order to be able to measure the transmission in the soft X-ray energy region, the samples must be made extremely thin and homogeneous.

Another way of measuring the absorption coefficient is by detecting the decay products of the absorption process itself. In Figure 4.3 beside the transmission mode two other ways of measuring the absorption process are depicted: the fluorescent yield and the total electron yield.

In the *fluorescent yield mode* one detects the electromagnetic radiation resulting from the radiative decay of the electrons from the occupied Density Of States (DOS) to refill the core hole created by the X-ray absorption process.

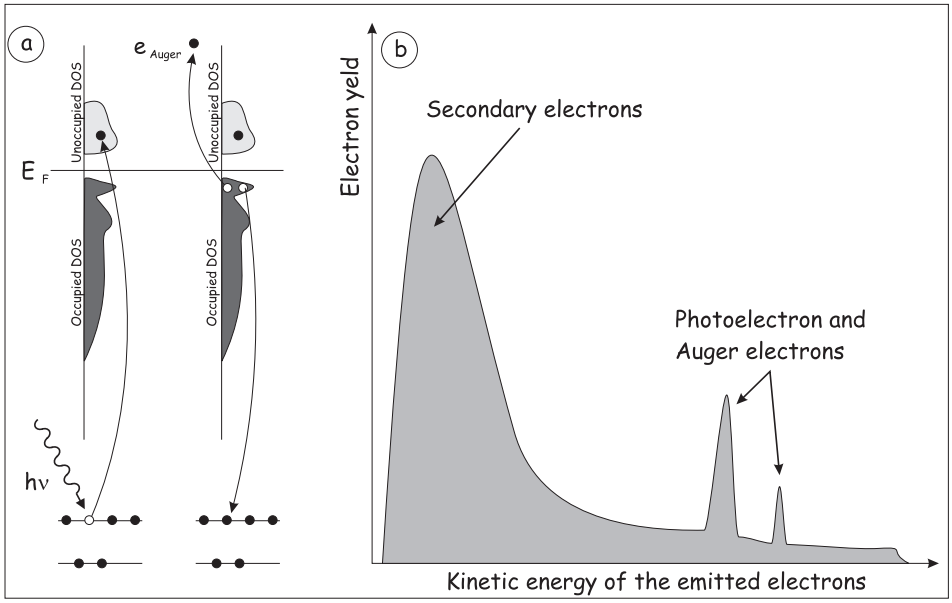

Figure 4.2: (a) Schematic figure of the absorption process. An core electron is excited by the incident X-rays into the unoccupied density of states (DOS) above the Fermi level. The measurement proceeds by detecting the decay products which can be photons, Auger electrons, photoelectrons or secondary electrons. (b) The energy distribution of these are decay products is presented.

The number of photons is proportional with the number of core holes created by the absorption process. This detection method proved to be more efficient and less demanding as far as the type of sample is concerned, since there is no limitation on the thickness of the sample contrary to the transmission mode nor has the sample to be conducting as is the case for the total electron yield mode (discussed later in this section). It is also important to note that this detection method is quite bulk sensitive since at these low photon energies there are almost no photon scattering processes: the probing depth of this technique is $\sim$2000 Å [15]. The drawback of this technique is that the mean free path of the fluorescent photons could be comparable to that of the incoming photons, hence self-absorption effects can take place, with the result that the fluorescent yield will no longer be proportional to the absorption coefficient. Moreover, the fluorescent process itself can be strongly dependent on the multiplet state that is created in the absorption process, making this technique less suitable for accurate quantitative measurements.

The last but most used detection method for the X-ray absorption process

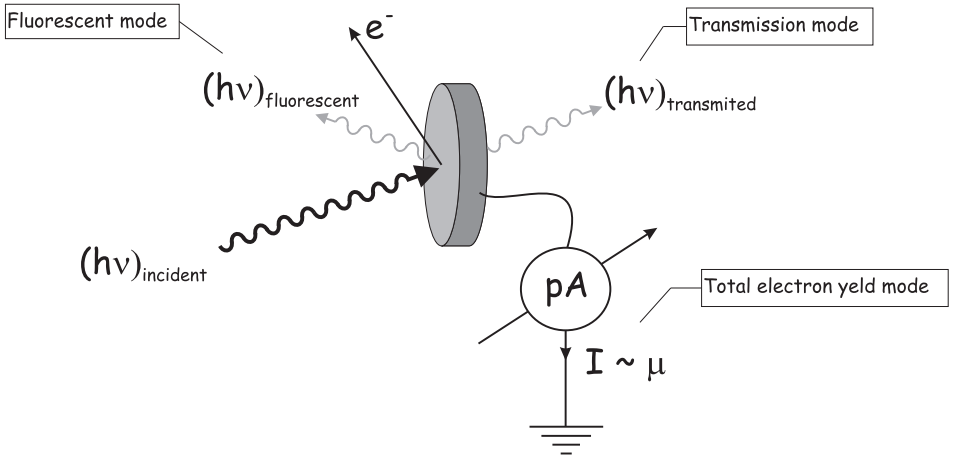

Figure 4.3: Measurement of the XAS spectra in the Total Electron Yield (TEY) mode. The absorbed photon creates a photoelectron which is emitted from a core level. The resulting core hole is later on occupied by a valence electron. The gained energy is transferred by Auger process to another electron which is emitted from the surface. The absorption is proportional to the number of electrons emitted thus also to the electrical current which neutralizes the sample. This drain current is measured as a function of photon energy and gives our XAS spectra.

is the *total electron yield mode* (TEY). What is measured here is the photoelectrical current which is supplied from the ground in order to neutralize the sample. Thus, as is depicted in Figure 4.3, the sample is grounded through a pico-amperemeter. Figure 4.2(a) exemplifies the processes that cause the "charging" of the sample: the unfilled core hole left behind by the X-ray absorption process is filled by an electron which decays from the occupied DOS, but in this case the process is not a radiative, but an Auger process. The energy gained from this decay is transferred to an other electron which can escape from the material. The leaving electron will conserve its kinetic energy only if is originating from not very deep under the surface, and this is due to the small elastic mean free path of the electrons in this energy region. Electrons originating from deeper regions of the sample will most probably suffer inelastic collisions and therefore will loose some of their kinetic energy. The photoemission spectrum of the electrons escaping from the irradiated surface is shown schematically in Figure 4.2(b). The amount of the so-called secondary electrons is orders of magnitude larger than the amount of the original Auger electrons, so experimentally it becomes very easy to measure

the decay products of the absorption process: the total electron yield can simply be measured by using a pico-amperemeter. However, it has been shown that the total electron yield signal is proportional to the absorption coefficient. The probing depth for this method is about 40-100 Å depending on material.

These two characteristics made TEY detection ideal for our purposes: the proportionality to the absorption coefficient allows for an accurate quantitative analysis of the spectra and the surface sensitivity is a necessity for ultra thin film samples.

In some cases when the material is very dense and the absorption is very high like in rare-earth elements, so that the escape depth of the electrons is comparable to the mean free path of the photons saturation effects may appear in the spectra. These effects were not of much importance for our transition metal oxide thin films and for further debate the reader is referred to [51].

In order to describe the XAS process one must know the ground state, the final state, and the matrix elements governing the transition cross section. Obviously, our aim is to find the ground state of the transition metal oxide film. The final state will be comprised by a core hole and an extra electron in the valence state. For the 2p-3d ($L_{2,3}$) transition the X-ray absorption process can be schematically represented as follows: $2p^6 3d^N + h\nu \rightarrow 2p^5 3d^{N+1}$. The probability of the electronic transition which actually gives us the absorption cross section is given by the Fermi golden rule:

$$\sigma \sim |\langle f|P|i\rangle|^2 \, \delta(E_f - E_i - \hbar\omega) \tag{4.1}$$

here $\langle f|P|i\rangle$ is the matrix element for the interaction between the *initial state* $|i\rangle$ and the *final state* $|f\rangle$. δ represents the requirement that the photon energy must match the energy difference between the possible electronic states. The operator P that couples the initial and final states can be written as:

$$P = e^{ik(\overrightarrow{\mathbf{n}}\cdot\mathbf{r})}\mathbf{p}\cdot\overrightarrow{\mathbf{e}} \tag{4.2}$$

where $\overrightarrow{\mathbf{e}}$ is the polarization vector and $\overrightarrow{\mathbf{n}}$ represents the propagation direction of the light and $\mathbf{r}$ is the electron position operator. Using the dipole approximation this operator is customary written as $P = \mathbf{p}\cdot\overrightarrow{\mathbf{e}}$, since only the first term is considered when expanding in series the exponential, here $\mathbf{p}$ is the momentum operator [40, 41]. The operator $\mathbf{p}$ can be replaced by the position operator $\mathbf{r}$ since $[\mathbf{r}, H] = (ih/m)\mathbf{p}$ [2]. It must be noted that the dipole approximation is valid since in this energy region since the wavelength of the soft X-ray radiation is much larger than the size of the atoms ($h\nu \in [100 - 1500]eV \Rightarrow \lambda \in [125 - 8.6]\mathring{A}$).

The final state, as shown in Figure 4.2(a) contains a core hole. However this core hole created by the incident photon will strongly interact with the valence electrons through the Coulomb interaction. Therefore, the process cannot be described in a one electron picture. In the case of transition metal oxides which are narrow band systems [42] the X-ray absorption is strongly excitonic since these strong Coulomb interactions are larger than the one electron bandwidth of the valence electrons, the electronic transition caused by the absorption process can be well described in an atomic-like picture [3, 5, 43, 46, 59]. A successful method to calculate the 2p-3d ($L_{2,3}$) spectrum is to consider a small cluster built up by a central transition metal atom surrounded by oxygen atoms located in such a way that they reflect the point symmetry of the transition metal atom in the crystal.

The number of existing initial and final multiplet states is a function of the number of d electrons, and this number can be very high already in the ionic limit (for the $2p^5 3d^5$ final state the number of possible terms is 1536). Figure 4.4 shows all available final states depending on the number of d electrons at the transition metal site. It is important to note that since the position operator $\mathbf{r}$ is an odd operator, the initial and the final states must have different parity, otherwise the integral in Equation 4.1 vanishes. The selection rules for the dipole transitions are:

$$\begin{aligned} \Delta l &= \pm 1 \\ \Delta m &= 0, \pm 1 \\ \Delta j &= 0, \pm 1 \\ \Delta L &= 0, \pm 1 \\ \Delta J &= 0, \pm 1 \\ \Delta S &= 0 \end{aligned} \tag{4.3}$$

All these rules are the so-called *dipole selection rules*. Satisfying these rules results in the pleasant surprise, namely, that not all possible final states presented in Figure 4.4 will be available and that the resulting XAS spectra will not be structure less.

The initial and final states of the atom are described by multiplets, which are multielectronic wavefunctions arising as a result of couplings of spin and angular momenta of the constituent electrons. For example the Russel-Saunders coupling results in such LS multiplet having terms of the form $^{2S+1}L_J$ with (2S+1) multiplicity. Each multiplet state has a certain atomic angular momentum quantum number J. Thus for an isolated atom each state is (2J+1)

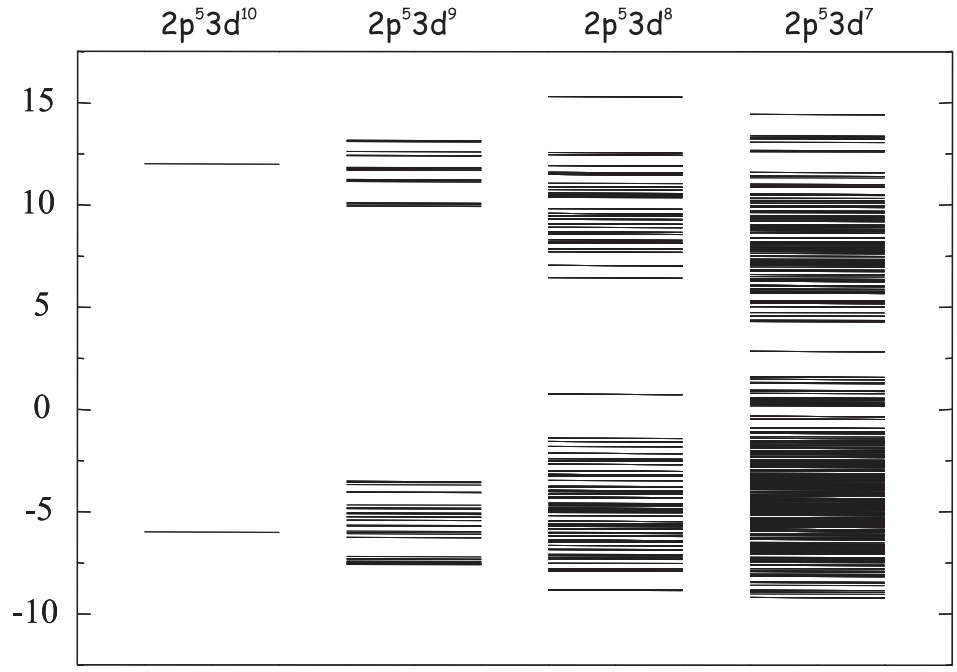

Figure 4.4: Multiplet structure in the final state $2p^5 3d^{N+1}$. Without the dipole selection rules all transitions to these states would be possible. Figure taken from ref. [46].

degenerate having $M_J = (-J, -J+1, \ldots, J-1, J)$ if there is no external magnetic field present. Taking in consideration all possible initial state multiplets ($2p^6 2d^N$) and final state multiplets ($2p^5 3d^{N+1}$), the transition probability can be calculated with Equation 4.1.

In the following we will present relevant examples illustrating some essential effects taken from the immense literature that appeared in the last 25-30 years after the prediction in 1985 [43] and experimental proof in 1986 [44] of strong magnetic X-ray dichroic effects.

4.4 Examples from literature

4.4.1 XAS of free atoms and solids

The first example presented here will be based on the findings of P. Gambardella *et al.* [45]. They reported XAS measurements on transition metal impurities on K and Na films. Here they were able to show that if transition

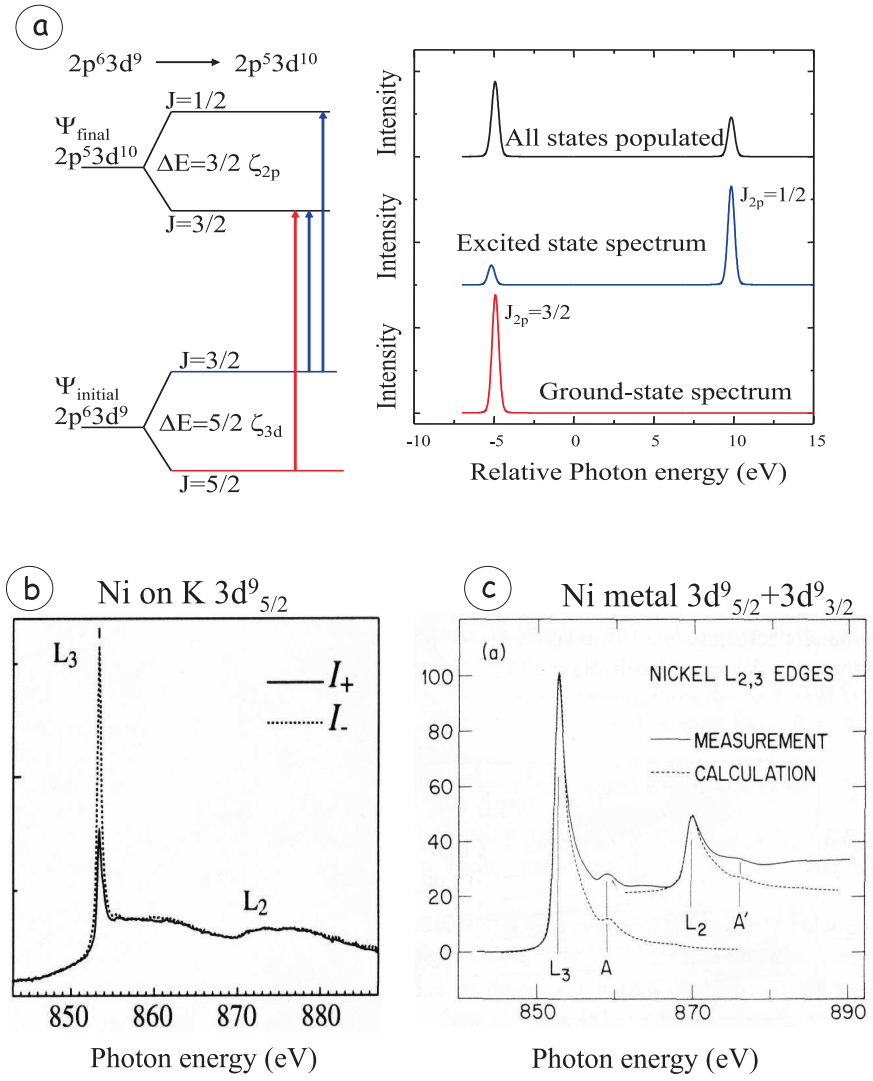

Figure 4.5: (a)(taken from ref [46]) (left) energy level diagram with initial and final states of the 2p-3d absorption process of Cu^{2+} or Ni $3d^9$. The initial state is the 3d spin orbit split ground state of which only the lowest part is occupied at very low temperatures in the atomic state. The final state is split by the core hole spin orbit interaction (several electronvolts in magnitude), (right) Calculated spectra depending on the population of the ground state.(b)(taken from ref [45]) XAS spectrum of Ni impurities on K film, only the L_3 edge is visible because in the ground state only the J=5/2 is populated and the dipole selection rules allow only $\Delta J = 0, \pm 1$. (c)(taken from ref [47]) XAS spectrum of Ni metal where both initial states are populated.

metal atoms are evaporated on these surfaces, such that they don't form clusters, they will exhibit atomic like character. The simplest example is Ni d^9. The XAS process is described by $2p^6 3d^9 \left|\alpha J M\right\rangle \rightarrow 2p^5 3d^{10} \left|\alpha' J' M'\right\rangle$ transition where the important quantum numbers are J and M, whereas α represents other quantum numbers. This example is convenient since in the final state only the p shell is unfilled since the d shell is complete. In this situation, for a free ion, according to Hund's rules, the ground state is described by a $^2D_{5/2}$ term. At an energy of $5/2{\cdot}\xi_{3d}$ above this ground level, where ξ_{3d} is the 3d spin-orbit coupling, lies the $^2D_{3/2}$ atomic level. For the final state the possible levels are $^2P_{3/2}$ and $^2P_{1/2}$ separated by $3/2{\cdot}\xi_{2p}$, where ξ_{2p} represents the 2p spin-orbit coupling (see also Figure 4.5(a)). In the atomic state, at very low temperatures, only the lowest lying level will be populated, therefore, taking into account the dipole selection rule $\Delta J = 0, \pm 1$, from the $^2D_{5/2}$ ground state only the $\Delta J = -1$ transition is possible hence only the $^2P_{3/2}$ state can be reached. This is represented by the bottom spectrum in Figure 4.5(a). The actual measurements are presented in Figure 4.5(b), one sees that only the transition from J=5/2 to J=3/2 occurs and that the L_2 edge is almost entirely suppressed.

In Ni metal both the states with J=5/2 and J=3/2 are instead populated due to both band formation and covalency. Therefore the transitions shown in Figure 4.5(a) (upper graph) are possible and the XAS spectrum of Ni metal has two peaks as seen in Figure 4.5(c), taken from ref [47].

4.4.2 X-ray circular dichroism

The use of synchrotron radiation provides not only a wide range of photon energies from which to choose, but it allows also to select of the light polarization. Therefore, one can use polarized light to probe only a specific part of the possible transitions. This is attainable since the photons have an angular momentum, namely q=±1 for circular and q=0 for linear polarized light. The polarization of the light is expressed in the $\vec{\mathbf{e}}$ vector of the dipole operator. Circularly polarized light is expressed as $\vec{\mathbf{e}}_{q=\pm 1} = \mp 1/\sqrt{2}(\vec{\mathbf{e}}_x + i\vec{\mathbf{e}}_y)$, and linearly polarized light as $\vec{\mathbf{e}}_{q=0} = \vec{\mathbf{e}}_z$. The dipole operator P can be thus expressed in spherical harmonics and this simplifies the calculation of integrals of the form of Equation 4.1. Depending on the polarization of the light, the dipole operator therefore be written as [48]:

$$P_{q=\pm 1} \quad = \quad r\sqrt{\frac{4\pi}{3}}Y_1^{\pm 1} \qquad \text{or,}$$

$$P_{q=0} = r\sqrt{\frac{4\pi}{3}}Y_1^0 \tag{4.4}$$

The magnetic quantum number M is changed according to the polarization of the impinging X-rays, such that $\Delta M = q$. The angular dependence of the absorption cross-section can be separated from the radial part such that the dependence of the absorption process on the light polarization becomes apparent. This is done using the Wigner-Eckart theorem (see for example the book of R.D. Cowan [49]), and σ becomes from Equation 4.1:

$$\sigma \sim \left|\left\langle f|P^{(1)}|i\right\rangle\right|^2 \cdot \begin{pmatrix} J & 1 & J' \\ -M & q & M' \end{pmatrix}^2 \tag{4.5}$$

where $\begin{pmatrix} J & 1 & J' \\ -M & q & M' \end{pmatrix}$ is the Wigner $3j$ symbol and $\left\langle f|P^{(1)}|i\right\rangle$ is the reduced matrix element of the dipole operator and gives the linestrength of the transition.

Shortly after the prediction and the experimental confirmation of the polarization dependent X-ray absorption, J.B. Goedkoop *et al.* published calculations of spectra for rare-earth compounds [50]. Figure 4.6 illustrates the energy levels involved in the absorption process for the simplest case: Yb^{3+}. The Ytterbium ion has 13 electrons in the 4f shell. According to Hund's rules this will result in ${}^2F_{7/2}$ ground state. The absorption process will excite a 3d electron to the only empty state in the 4f shell, thus the final state will become $3d^9 4f^{14}$, which again according to Hund's rules is the ${}^2D_{5/2}$. In the atomic state, without any magnetic field present, the transition with $\Delta J = -1$ is the only possible one. This case is depicted in the left side of Figure 4.6. When the ion is placed in a nonzero magnetic field the $2 \cdot 7/2 + 1 = 8$ fold degeneracy is lifted and the sub-levels are split by the Zeeman energy of $E_M = -\mu g_J \mathbf{H} M$. Depending on the polarization of the incident photons, three different groups of transitions exist as depicted in the right side of the energy-level diagram. Since the splitting of the Zeeman levels is of the order of $\sim$1 meV at high temperatures all levels will be equally populated, thus no effect of the dichroism will be visible. At low temperatures, however, the effect of the Boltzmann distribution on the occupation of these levels will cause an unequal absorption for different ΔM_j groups. At T=0K only the M=-7/2 will be populated therefore only absorption of light with polarization q=1 is possible. At the bottom of the figure the relative intensity is plotted as calculated from the squared values of the 3j symbols for the specific transitions. Formulas giving this dependence on the specific values of J and M can be found in many references [40, 50, 52, 54].

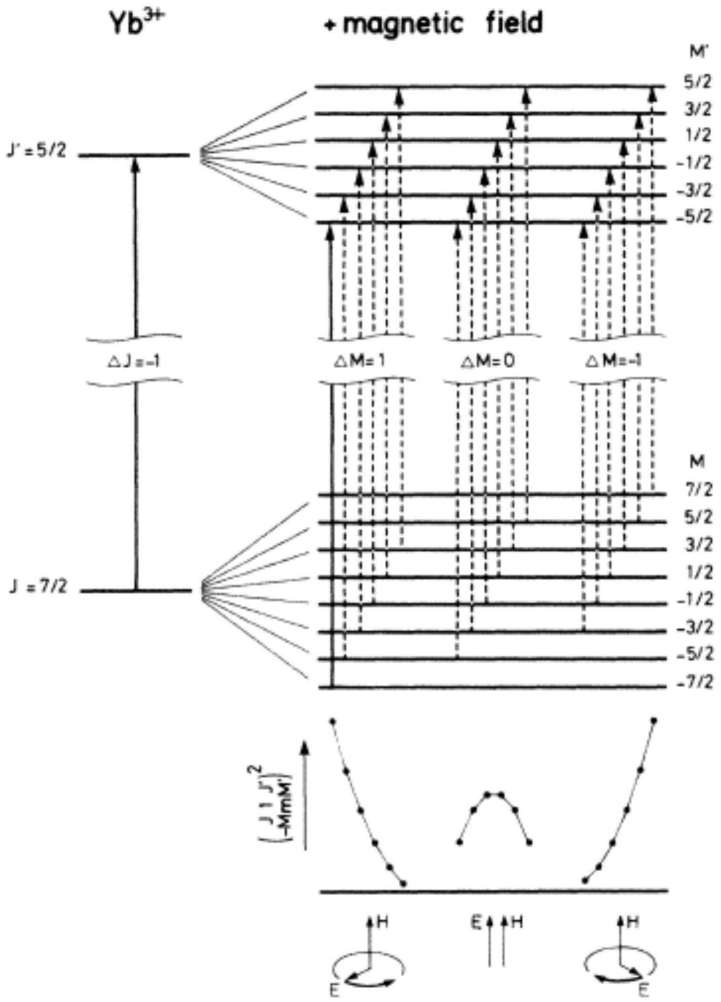

Figure 4.6: Energy level diagram for trivalent Ytterbium. On the left side the free ionic levels involved in the absorption process are shown , while on the right side the splitting due to the magnetic field becomes apparent. The energy scale in the figure is not on scale, the Zeeman splitting being very small, of the order of $\sim$ 1 meV. Figure taken from ref. [50].

Historically, after these developments focusing only on rare earth compounds, the first experimental circular dichroic experiment on 3d transition metals was done by C.T. Chen and co-workers [9] who studied the circular dichroism of Ni metal, presented in Figure 4.7.

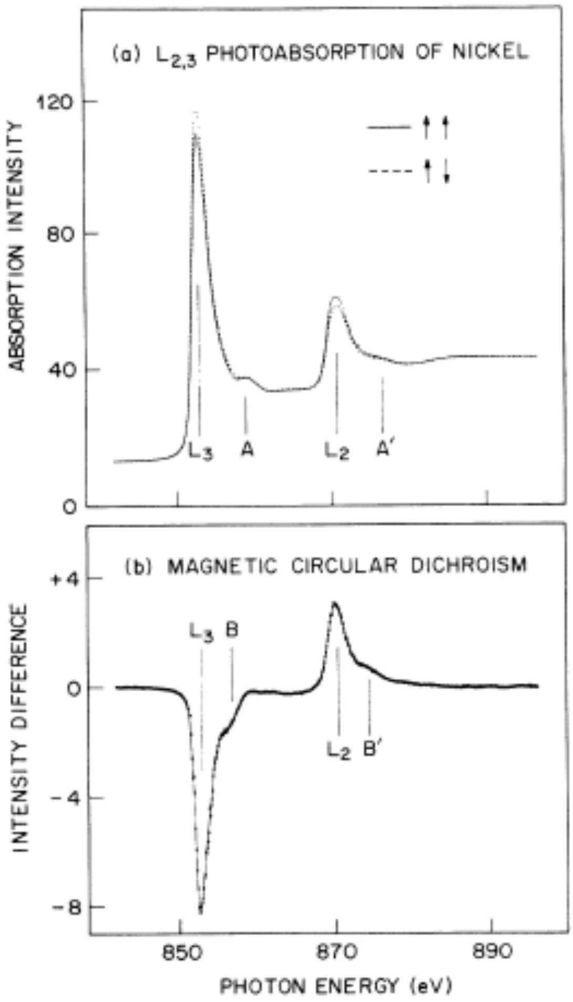

Figure 4.7: (a) X-ray absorption spectra of Ni metal taken with two different polarizations of the X-ray photons with respect to the spin direction. (b) Difference spectrum (Magnetic Circular Dichroism). Figure taken form ref. [53].

In ferromagnets the net magnetization is caused by lowering of the energy by parallel alignment of neighboring spins (*exchange energy*). Therefore, electronic states with m_j corresponding to a certain spin orientation will be preferentially occupied (the highest unoccupied state being the $m_j = 3/2$). Thus, considering the absorption cross-section from the calculation of the square of

the 3j symbols, one would expect the following ratios: $\sigma_{L_3tot}/\sigma_{L_2tot} = 2:1$ and $\frac{MCD_{L_3}}{MCD_{L_2}} = -1:1$. In reality the ratios measured were 2.6:1 and -1.6:1, respectively. Subsequent analysis has shown that these deviations from the statistical expectations are caused by the spin-orbit interaction active in the Ni 3d shell, i.e. that the Ni carries an orbital momentum. These results clearly show that the dichroic signal is sensitive to small details of the electronic and magnetic structure.

As we have seen, the line shape and intensity of the X-ray absorption spectrum depend on relative orientation of the photon angular momentum and the magnetization direction. This can be achieved for ferromagnetic samples where the net magnetic moment of the material is nonzero: $\langle \mathbf{M} \rangle \neq 0$. On the other hand, for antiferromagnets where the net magnetization is zero (or very small even in high external magnetic fields) there will be no (or very little) circular dichroism. However, linear dichroism, which is the difference in intensity or shape of the spectrum with the antiferromagnetic axis aligned *parallel* or *perpendicular* with the polarization axis, exists also in the case of antiferromagnets. Here the important quantity is the mean of the square of the magnetization ($\langle \mathbf{M}^2 \rangle \neq 0$). Thus in the following sections we will give some examples that deal with different linear dichroic effects.

4.4.3 X-ray magnetic linear dichroism

In this section we focus on the two classic experimental papers by Kuiper *et al.* [19] and Alders *et al.* [21] which constitute important milestones in the field on linear dichroism of antiferromagnetic materials.

In Figure 4.8 is presented the XAS spectrum of Fe_2O_3 antiferromagnet taken below and above the so-called Morin transition which occurs at ∼263 K. This magnetic phase transition manifests itself as a change of direction of the magnetic moments with respect to the trigonal c axis of the corundum structure of Fe_2O_3. In both cases the spectra are taken with the c axis parallel to the polarization direction of the incident X-rays and thus the difference in the spectra is entirely due to the change in orientation of the magnetic moments on the Fe sites. Fe_2O_3 with the Fe^{3+} ions having 5 high spin electrons in the 3d orbitals, has an atomic ground state $^6S_{5/2}$. This is an orbital singlet (L=0), thus the ground state has A_{1g} symmetry. Hence such a high polarization dependence can not be the result of a deformation of the oxygen octahedra (final state effects). At very low temperatures in a magnetic field, the J=5/2 level of the free ion is split into six Zeeman sub-levels and the ground state level m_j=-5/2 is occupied. Using linearly polarized light with the electric field vector aligned along the magnetic moments, the selection rule

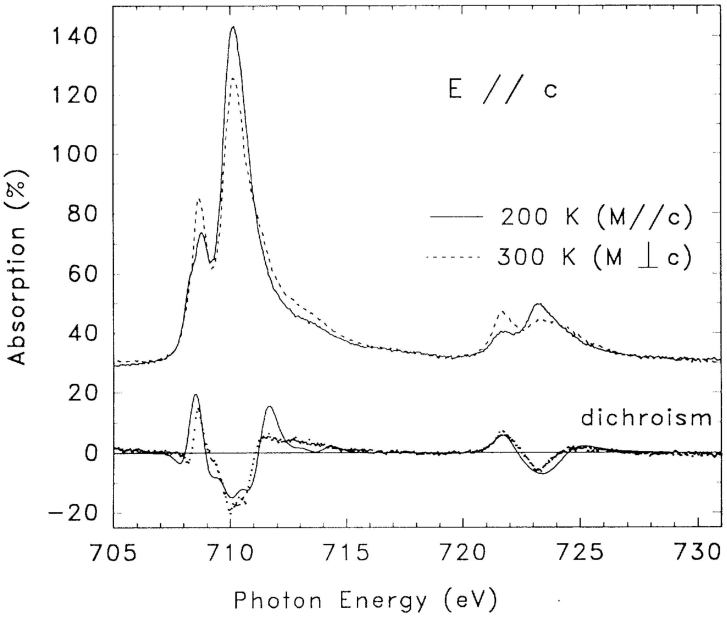

Figure 4.8: X-ray absorption spectra taken below (T=200K) and above (T=300K) the Morin transition (T=$\sim$ 263K) using polarized X-rays with the electric field vector parallel with the c axis. Figure taken form ref. [19].

Δm=0 restricts the transitions from the initial J=5/2, to states having J'=7/2 and J'=5/2 since only these have m'_j=5/2 sub-levels. When the electric field vector of the linearly polarized X-rays is perpendicular to the magnetic moments also the J'=3/2 levels can be reached, since this polarization carries Δm=-1. This causes the large difference observed between the spectra taken below and above the Morin transition.

The other classical example is the work of D. Alders *et al.* [21, 54]. Here the authors present a detailed analysis of thickness as well as temperature dependent X-ray magnetic linear dichroism of NiO thin films.

In NiO thin films epitaxially grown on MgO (001) the largest changes in the spectrum as a function of polarization were observer at the Ni L_2 edge (see Figure 4.9(a)). By comparing the calculated spectrum with the experimental one it was further shown that the ratio of the two components of the L_2 edge scales linearly with the exchange field. Therefore, this ratio of the two peaks served as a measure for the nearest neighbor spin-spin correlation function. The spectrum which for the sake of clarity is normalized to the first peak of the L_2 edge shows a change of the ratio of the order of 40 %. The variation of

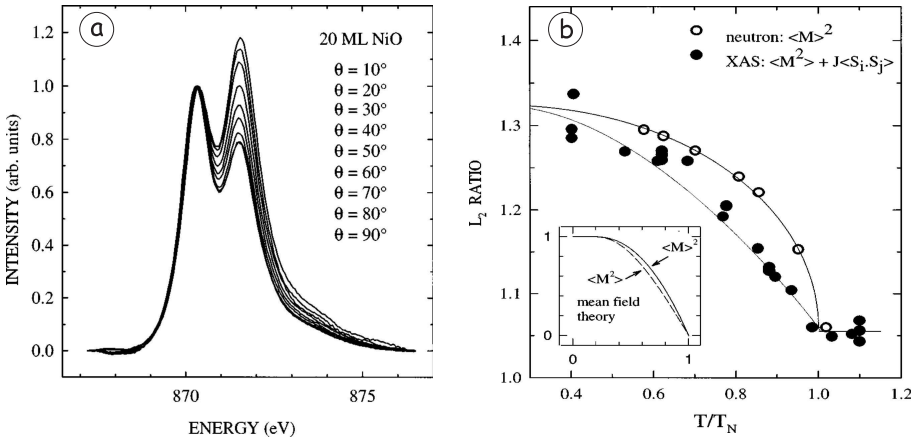

Figure 4.9: (a) Angular dependent Ni L_2 edge spectrum of 20 ML NiO thin film on MgO (100). (b) Ratio of the two peaks as a function of temperature, compared with neutron diffraction data taken from ref. [55]. Figure taken form ref. [21].

this ratio of the two peaks as a function of temperature, is presented in Figure 4.9 (b) and compared with the neutron diffraction data taken from ref [55]:

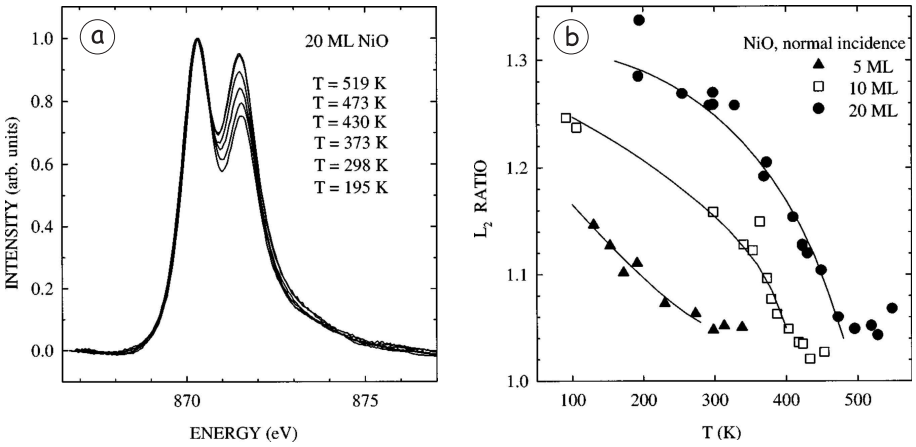

Figure 4.10: (a) Temperature dependent Ni L_2 edge spectrum of 20 ML NiO thin film on MgO (100). Ratio of the two peaks at the L_2 edge for films having different thickness. The 5 ML film has a Neél temperature close to room temperature. Figure taken form ref. [21].

while neutron diffraction measures the mean of the local magnetization $\langle \mathbf{M} \rangle$, XAS technique measures the mean of the square of the magnetization $\langle \mathbf{M}^2 \rangle$ plus the exchange field from the nearest neighbor spin-spin correlation function $J \langle \mathbf{S}_i \cdot \mathbf{S}_j \rangle$. From the comparison of the experimental with the calculated spectrum, it was also determined that for the NiO films, the easy axis of the spins on the Ni site is parallel to one of the [±2,±1,±1] crystallographic directions. Here we must note that spin-orbit coupling is crucial for the appearance of magnetic linear dichroism. In fact for O_h symmetry no orbital ordered state is expected (*no initial state effects*) and the absorption cross-section is independent of polarization. Therefore, MLD can occur only by some coupling of the electronic part with the spin part of the wavefunction. This coupling is exactly the spin-orbit coupling (see for more ref. [46]).

The temperature dependence of the spectrum also changes with the thickness of the NiO film as shown in Figure 4.10. For thinner films the temperature at which antiferromagnetic order is still present is lower. For the 5 ML NiO films on MgO the Néel temperature is only ∼295 K, i.e. less than 2/3 of the bulk value of 520 K. As we will show in Chapter 6 such an effect is not observed, for identically thin layers of CoO on MnO where the Néel temperature is the same as for the bulk.

4.4.4 The effects of the crystal fields

The electronic and magnetic properties of the materials are a direct consequence of the behavior of the outermost uncomplete electronic shells. Transition metals have open d shells while rare earths have open f shells. Therefore, the main interest focuses on these electrons. A change in environment, like a change in the atomic distances or a deformation of the distribution of the closest lying anions, will result in a change of the electron configurations of these ions. Since this electron configuration determines the electronic and magnetic properties of these materials, we are mainly interested in how, by altering the natural environment, we are able to change or even control of these properties. In order to achieve this, a closer look at this anion environment is appropriate.

In the rock-salt transition metal oxides such as CoO and MnO, studied in the following chapters, the metal cation is surrounded by an octahedra formed by the six oxygen anions as presented in Figure 4.11. In a free atom the atomic d levels are all degenerate, (they have the same energy and they are spherically symmetric), but once embedded in this cubic environment some d orbitals will be energetically more favorable than others. Figure 4.11 exemplifies this statement. Depending on their orientation with respect to the anions, the

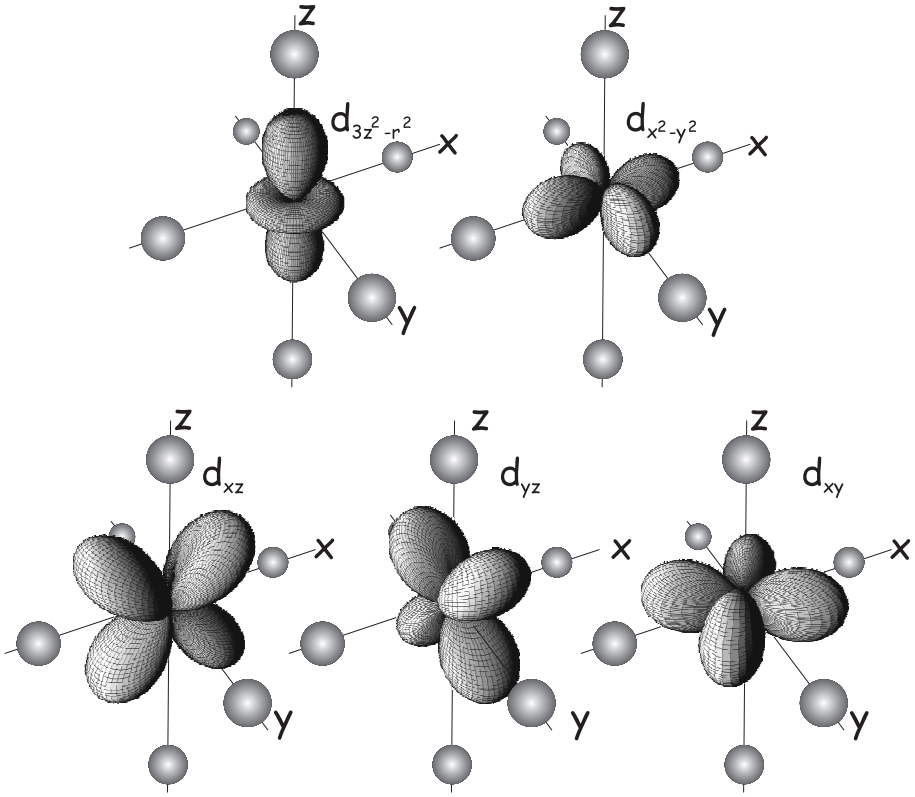

Figure 4.11: Schematic figure of d orbitals in an octahedral field of anions. It is here visible that the $d_{3z^2-r^2}$ and the $d_{x^2-y^2}$ orbitals point toward the anions while the d_{xy}, d_{xz} and d_{yz} orbitals point in between the anions. This is the reason for the energy splitting between the upper group and the lower group, namely between the e_g and the t_{2g} energy levels.

d orbitals will split into the lower lying triply degenerate t_{2g} orbitals, which point *in between* the anions, and the higher lying e_g orbitals which point *towards* the anions. The occupation of these orbitals will proceed in such a way that the overall energy will be minimal. In a simple picture there are two concurring effects which play a role in the population of these orbitals, the exchange interaction which minimizes the energy if two electrons are parallel and the crystal field splitting which favors the occupation of the lower t_{2g} orbital. If the crystal field splitting is small, the electrons will arrange as to maximize the spin. If the crystal field is large, the electrons will tend to stay in the lower t_{2g} orbitals, i.e. in the low spin configuration. In some cases the

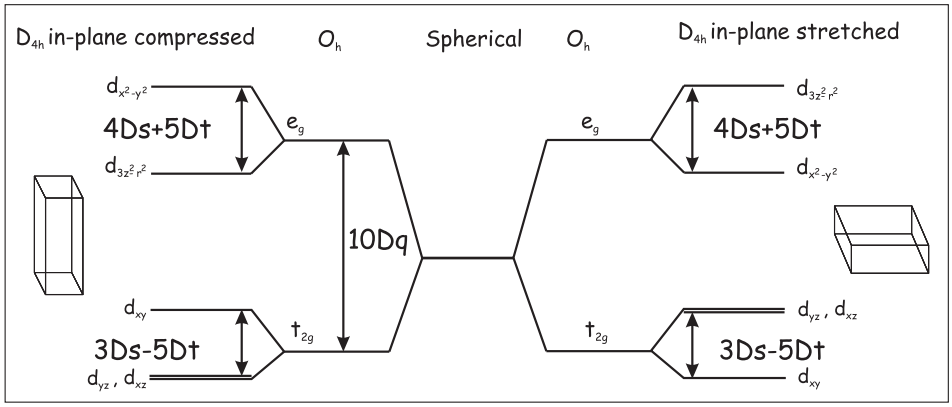

Figure 4.12: Energy level diagram of the d levels for a transition metal atom in an octahedral filed (middle) or in a tetragonally distorted octahedra (left and right).

so-called intermediate spin state is possible where both effects are comparable in size (see for details ref. [51]).

If the octahedra are tetragonally distorted, the symmetry decreases from O_h to D_{4h} and results in a further splitting of the initially so-called t_{2g} and e_g levels. Two extra parameters Ds and Dt are needed for describing this splitting. The reason why they are called parameters is because they are used together with Dq as empirical parameters when fitting the measurements. Theoretical calculations of these parameters were not very successful. All these quantities depend on the radial part of the wavefunctions and therefore the covalent mixing of the metal and ligand orbitals have a major contribution to them also. Figure 4.12 presents a simple overview of the energetics if the levels as a cause of the two kinds of tetragonal distortion of the octahedra.

4.4.5 Initial state effects

X-ray absorption using linearly polarized light is very sensitive also to orbital occupation. This is easily put in evidence by the following example regarding the dipole allowed K edge absorption from s orbital to p orbital. With linearly polarized light the absorption process which is given by Equation 4.1, is described by the integral of the form $\left\langle i \left| r\sqrt{\frac{4\pi}{3}}Y_1^0 \right| f \right\rangle$, which, by replacing $Y_1^0 = \sqrt{\frac{3}{4\pi}}\frac{z}{r}$, results in the simple integral $\langle i|z|f\rangle$. This integral can only be nonzero if the product of the three functions is even. Being now concerned

with the absorption from an s orbital (which is even) to a p orbital (which is an odd function in x, y or z variables), the product of the three will only be even if the polarization of the X-rays matches the orientation of the p orbital. Therefore, one can excite from an s level into a p_z orbital only with z polarized light and into a p_x orbital with x polarized light. A generalization of this example is the statement: *since the dipole operator* $\boldsymbol{r}$ *is a vector with components (x, y, z), the dipole transition will be allowed if the direct product of the irreducible representations of the initial and final states is or contains the irreducible representations to which x, y, or z belongs* [41].

A revealing result for a slightly different case, namely the case of specific type of holes in the 3d orbitals, is presented in Figure 4.13. Here polarization dependent X-ray absorption of $La_{1.85}Sr_{0.15}CuO_4$, a high T_c superconductor, is reproduced from ref. [15]. The authors (C.T. Chen *et al.*) were able to elucidate the controversy that appeared around the amount of O $2p_z$ versus the O $2p_{x,y}$ character as well as the Cu $3d_{3z^2-r^2}$ versus the Cu $3d_{x^2-y^2}$ hole character in these high temperature superconductive compounds which attracted much interest. The specific measuring geometry allowed for an easy and transparent procedure for data analysis and we shall follow a similar procedure for our experiments as detailed in the following two chapters. Until the appearance of this paper there was no transparent way of deriving what percentage of Cu 3d holes (which are responsible for the conduction), are $d_{3z^2-r^2}$ in character.

In Figure 4.13 is very clear that there is a strong difference in absorption as a function of the orientation of the electric field vector with respect to the c axis. The latter is perpendicular to the CuO_2 planes in this material. While the electrical field vector is parallel with the c axis (perpendicular to the CuO_2 planes) the absorption is almost entirely suppressed which clearly suggests that the 3d holes lie in the plane. The holes therefore reside mainly in the Cu $3d_{x^2-y^2}$ orbitals. The calculated value for the Cu $3d_{3z^2-r^2}$ hole character was determined to be $\sim$1.5%.

4.4.6 Final state effects

In one of the previous sections we shortly discussed the results of D. Alders *et al.* about MLD of NiO epitaxial thin films on MgO. We pointed out that thinner films have lower Néel temperatures than thicker films ($\sim$ 20 ML) which had Néel temperatures close to the bulk value. In this final section we want to turn the reader's attention to an instructive example discussed by M.W. Haverkort *et al.* [60]. These authors report XAS measurements from 1 ML NiO epitaxial film grown on Ag (100) single crystals, the film being capped by a 10 ML MgO (100) layer. As it was already discussed in Chapter 3 of

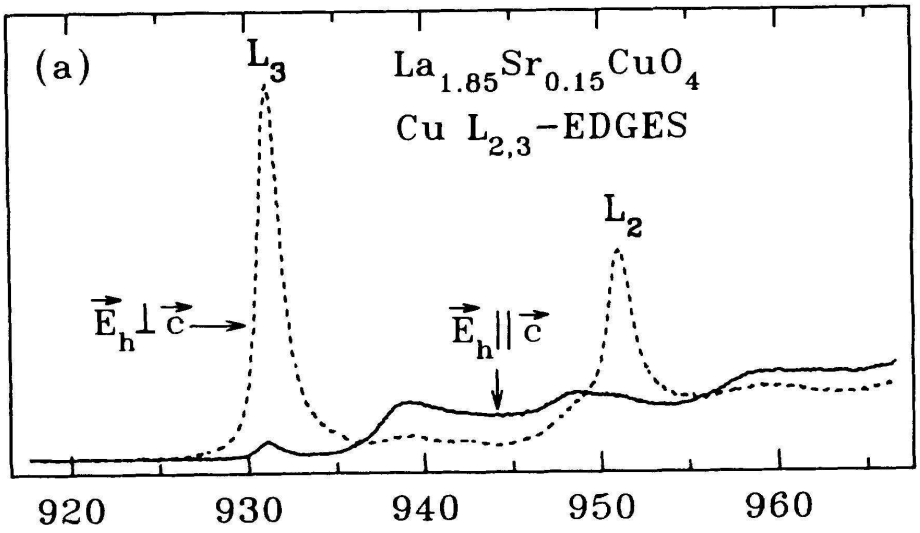

Figure 4.13: Cu $L_{2,3}$ XAS spectra showing immense difference in absorption for the two polarizations. The 3d hole in the Cu $3d^9$ ion resides almost entirely in the $d_{x^2-y^2}$ orbitals. Figure taken form ref. [15].

this thesis, very thin epitaxial films, with a certain amount of misfit, will grow homogeneously on the substrate and they will contain a considerable amount of tetragonal distortion imposed by the substrate. Observing the trend of the Neel temperature with decreasing thickness of the films, one would expect, as the authors also confirm, that the ordering temperature, if any, of 1 ML NiO is lower than room temperature. Even so, for this very thin film a clear linear dichroism was observed at room temperature as well as an energy shift of the peak at the Ni L_3 edge, as can be seen from Figure 4.14(a).

The linear dichroism observed was attributed entirely to the lowering of the symmetry of the Ni atoms, from a perfect octahedron (O_h point group symmetry) to a tetragonally deformed one (in-plane compressed and out-of-plane elongated D_{4h}). This scenario was illustrated in detail in the previous section 4.4.4, in the left side of Figure 4.12. A very simple explanation of the energy shift as well as the slight change in intensity is the following. In a one electron picture, Ni^{2+} has 8 d electrons, thus the high-spin ground state will consist of two holes occupying the $3d_{x^2-y^2}$ and the $3d_{3z^2-r^2}$ orbitals. The absorption process using z-polarized light will promote a 2p electron to the $3d_{3z^2-r^2}$ orbital but not to the $3d_{x^2-y^2}$ orbital because of reasons explained in Section 4.4.5. Changing the polarization of the X-rays to x, mainly the $3d_{x^2-y^2}$

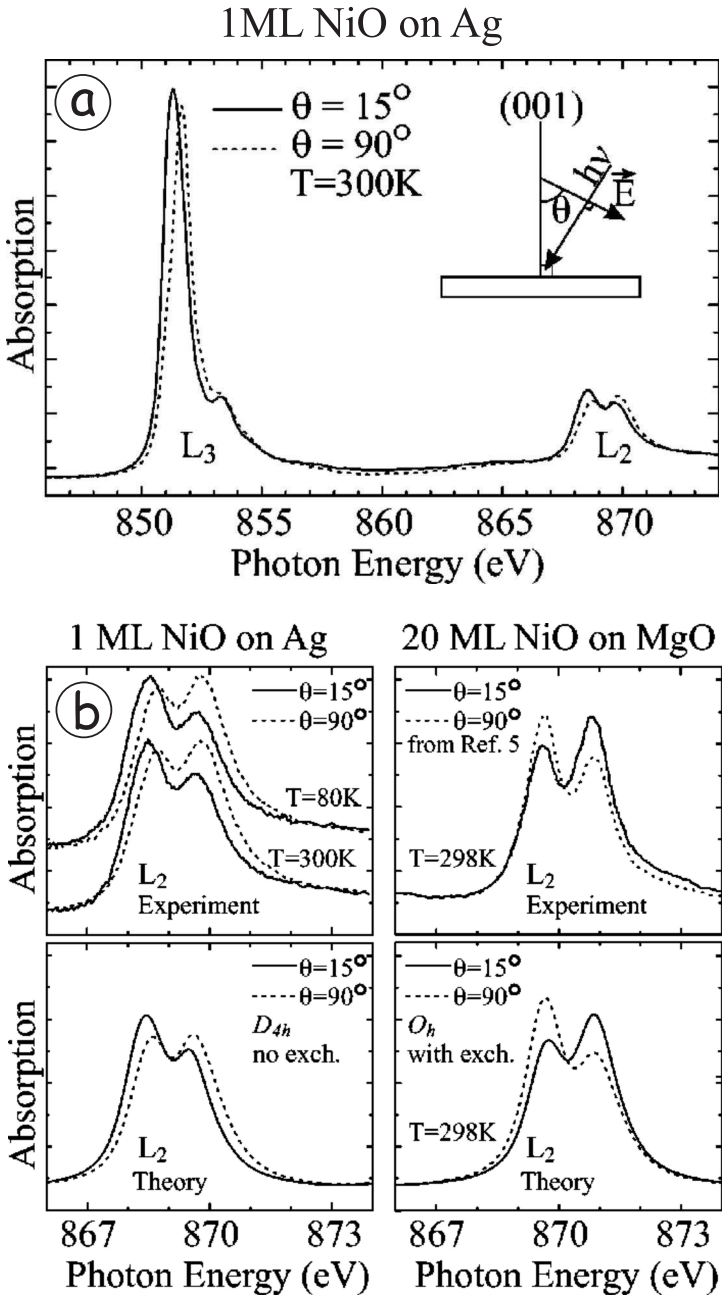

Figure 4.14: (a) Linear dichroism detected at the Ni $L_{2,3}$ edge from 1 ML NiO film on Ag (100). (b) Comparison of linear dichroism at the Ni L_2 edge of 1 ML NiO on Ag and 20 ML NiO on MgO. Figures taken form ref. [60].

orbitals will be reached. The exact final state in this case will be $2p^5\underline{3d}_{z^2-y^2} = \sqrt{3/4}(2p^5\underline{3d}_{3z^2-r^2}) + \sqrt{1/4}(2p^5\underline{3d}_{x^2-y^2})$ where the underline represents a hole. However, one can see from Figure 4.12 that the $3d_{3z^2-r^2}$ energy level is lower than the $3d_{x^2-y^2}$ thus the $2p^5\underline{3d}_{x^2-y^2}$ final state will be $4Ds + 5Dt$ lower than the $2p^5\underline{3d}_{3z^2-r^2}$ state. This is exactly the energy difference that is measured by the difference of the position of the peak at the Ni L_3 edge in Figure 4.14(a). Moreover, the authors have also presented theoretical spectra with and without the inclusion of an exchange field simulating the existence and the absence of magnetic ordering. They found that the spectra from 1 ML NiO on Ag can be described very well using only a D_{4h} point group and no exchange, thus without any magnetic ordering present in the film.

This study exemplifies very convincingly that final state effects can also produce strong dichroism, thus one must be careful when attributing the observed dichroic effects as results of magnetic ordering. There is a similar situation for the case of epitaxial MnO layers on Ag (100), as will be presented in more detail in Chapter 6.

4.5 Conclusions

In this chapter we discussed the X-ray absorption technique by the use of examples from the available literature. We have demonstrated that XAS can give insight not only in ferromagnets but also in antiferromagnets. We have also shown that one-electron picture can be very useful in qualitative explanations but eventually one has to use the full atomic cluster calculations in order to get quantitative results. For more details about such calculations we refer the reader to the PhD thesis of M.W. Maurits [46]. This chapter was ment to be an introductory chapter for the rest of this thesis where we will deal with the changes in the magnetic structure of CoO and MnO as a result of strain and interlayer coupling.

References

[1] For a review see: 'Unoccupied Electronic States', 'Fundamentals for XANES, EELS, IPS, and BIS', edited by J.C. Fuggle and J.E. Inglesfield, Topics in Applied Physics, Vol. 69 (Springer Verlag, Berlin 1992)

[2] See review by F. M. F. de Groot, J. Electron Spectrosc. Relat. Phenom. **67**, 529 (1994).

[3] A. Tanaka and T. Jo, J. Phys. Soc. Jpn. **63**, 2788 (1994).

[4] See review in the Theo Thole Memorial Issue, J. Electron Spectrosc. Relat. Phenom. **86**, 1 (1997).

[5] B.T. Thole, R.D. Cowan, G.A. Sawatzky, J. Fink, J.C. Fuggle, Phys. Rev. B **31**, 6856 (1985)

[6] J. Fink, Th. Müller-Heinzerling, B. Scheerer, W. Speier, F.U. Hillebrecht, J.C. Fuggle, J. Zaanen and G.A. Sawatzky, Phys. Rev. B **32**, 4899 (1985)

[7] J. Fink, Advances in Electronics and Electron Physics **75**, 121 (1989)

[8] J. Fink, in 'Unoccupied Electronic States', 'Fundamentals for XANES, EELS, IPS, and BIS', edited by J.C. Fuggle and J.E. Inglesfield, Topics in Applied Physics, Vol. 69 (Springer Verlag, Berlin 1992), p. 203

[9] C.T. Chen and F. Sette, Phys. Scripta **T31**, 119 (1990)

[10] G. van der Laan, B.T. Thole, G.A. Sawatzky, and M. Verdaguer, Phys. Rev. B **37**, 6587 (1988)

[11] C. Cartier dit Moulin, P. Rudolf, A.-M. Flank, and C.-T. Chen, J. Phys. Chem. **96**, 6196 (1992).

[12] M. Abbate, J.C. Fuggle, A. Fujimori, L.H. Tjeng, C.T. Chen, R. Potze, and G.A. Sawatzky, Phys. Rev. B **47**, 16124 (1993)

[13] M. Abbate, R. Potze, G.A. Sawatzky, C. Schlenker, H.J. Lin, L.H. Tjeng, C.T. Chen, D. Teehan, and T.S. Turner, Phys. Rev. B **51**, 10150 (1995)

[14] H.F. Pen, L.H. Tjeng, E. Pellegrin, F.M.F. de Groot, G.A. Sawatzky, M.A. Veenendaal, and C.T. Chen, Phys. Rev. B **55**, 15500 (1997)

[15] C.T. Chen, L.H. Tjeng, J. Kwo, H.L. Kao, P. Rudolf, F. Sette, and R.M. Fleming, Phys. Rev. Lett. **68**, 2543 (1992)

[16] N.L. Saini, S. Venkatesh, P. Srivastava, B.R. Sekhar, K.B. Garg, L.H. Tjeng, C.T. Chen, A. Menovsky, and J.J.M. Franse, J. Phys.:Condens. Matter **8**, 2467 (1996)

[17] J.-H. Park, L.H. Tjeng, J.W. Allen, C.T. Chen, P. Metcalf, J.M. Honig, F.M.F. de Groot, and G.A. Sawatzky, Phys. Rev. B **61**, 11506 (2000)

[18] T. Mizokawa, L.H. Tjeng, P.G. Steeneken, N.B. Brookes, I. Tsukada, T. Yamamoto, and K. Uchinokura, Phys. Rev. B. (accepted)

[19] P. Kuiper, B.G. Searle, P. Rudolf, L.H. Tjeng, and C.T. Chen, Phys. Rev. Lett. **70**, 1549 (1993)

[20] D. Alders, J. Vogel, C. Levelut, S.D. Peacor, T. Hibma, M. Sacchi, L.H. Tjeng, C.T. Chen, G. van der Laan, B.T. Thole, and G.A. Sawatzky, Europhys. Lett. **32**, 259 (1995)

[21] D. Alders, L.H. Tjeng, F.C. Voogt, T. Hibma, G.A. Sawatzky, J. Vogel, M. Sacchi, S. Iacobucci, and C.T. Chen, Phys. Rev. B **57**, 11623 (1998).

[22] P. Rudolf, F. Sette, L.H. Tjeng, G. Meigs, and C.T. Chen, J. Magn. Magn. Mater. **109**, 109 (1992)

[23] L.H. Tjeng, Y.U. Idzerda, P. Rudolf, F. Sette, and C.T. Chen, J. Magn. Magn. Mater. **109**, 288 (1992)

[24] J. van Elp, S.J. George, J. Chen, G. Peng, C.T. Chen, L.H. Tjeng, G. Meigs, H.-J. Lin, Z.H. Zhou, M.W.W. Adams, B.G. Searle, and S.P. Cramer, Proc. Natl. Acad. Sci. USA **90**, 9664 (1993)

[25] Y.U. Idzerda, C.J. Gutierrez, L.H. Tjeng, H.-J. Lin, G. Meigs, and C.T. Chen, J. Magn. Magn. Mater. **127**, 109 (1993)

[26] Y.U. Idzerda, L.H. Tjeng, H.-J. Lin, C.J. Gutierrez, G. Meigs, and C.T. Chen, Phys Rev. B **48**, 4144 (1993)

[27] C.T. Chen, Y.U. Idzerda, C.-C. Kao, L.H. Tjeng, H.-J. Lin and G. Meigs, Mat. Res. Soc. Symp. Proc. Vol. **375**, 59 (1995)

[28] C.T. Chen, Y.U. Idzerda, C.-C. Kao, L.H. Tjeng, H.-J. Lin, and G. Meigs, Materials Science and Engineering B **31**, 49 (1995)

[29] Y.U. Idzerda, C.T. Chen, H.-J. Lin, L.H. Tjeng, and G. Meigs, Physica B **208&209**, 746 (1995)

[30] E. Pellegrin, L.H. Tjeng, F.M.F. de Groot, R. Hesper, G.A. Sawatzky, Y. Moritomo, and Y. Tokura, J. Electron Spectrosc. Relat. Phenom. **86**, 115 (1997)

[31] B.T. Thole, P. Carra, F. Sette, and G. van der Laan, Phys. Rev. Lett. **68**, 1943 (1992)

[32] P. Carra, B. T. Thole, Massimo Altarelli, and Xindong Wang, Phys. Rev. Lett. **70**, 694 (1993)

[33] C.T. Chen,Y. U. Idzerda, H.-J. Lin, N. V. Smith, G. Meigs, E. Chaban, G. H. Ho, E. Pellegrin, and F. Sette, Phys. Rev. Lett. **75**, 152 (1995)

[34] K. Wille, Rep. Prog. Phys. **54**, 1005 (1991)

[35] D. Attwood, *Soft x-rays and extreme ultraviolet radiation: Principles and applictaions*, Cambridge University Press, Cambridge (1999)

[36] C.T. Chen, Nucl. Instrum. Methods, **256**, 595 (1987)

[37] C.T. Chen and F. Sette, NSLS Annual Report, 2-16 (1987)

[38] C.T. Chen and F. Sette, Rev. Sci. Instrum. **60**, 1616 (1989)

[39] *X-ray data booklet*, University of California, California (2001)

[40] J. Goedkoop, *X-ray dichroism of rare earth materials*, PhD thesis, Nijmegen (1989)

[41] J. Stöhr, *NEXAFS Spectroscopy*, Springer-Verlag, Berlin (1992)

[42] P.A. Cox, *Transition Metal Oxides*, Oxford (1995)

[43] B.T. Thole, G. van der Laan, J.C. Fuggle, G.A. Sawatzky, R.C. Karnatak, J.-M. Esteva, Phys. Rev. B, **32**, 5107 (1985)

[44] G. van der Laan, B.T. Thole, G.A. Sawatzky, J.B. Goedkoop, J.C. Funggle, J.-M. Esteva, R. Karnatak, J.P. Remeika, H.A. Dabkowska, Phys. Rev. B, **34**, 103 (1986)

[45] P. Gambardella, S.S. Dhesi, S. Gardonio, C. Grazioli, P. Ohresser, and C. Carbone, Phys. Rev. Lett. **88**, 047202 (2002)

[46] M.W. Maurits, *Spin and orbital degrees of freedom in bulk and thin film transition metal ixides studied by 2p core level X-ray absorption spectroscopy*, PhD thesis, Köln (2005)

[47] C.T. Chen, N.V. Smith, F. Sette, Phys. Rev. B, **43**, 6785 (1991)

[48] R. Nakajima, *X-ray magnetic circular dichoism spectroscopy in transition metal thin films*, PhD. thesis, Stanford University (1998)

[49] R.D. Cowan *The theory of atomic structure and spectra*, University of California Press, Berkeley (1981).

[50] J.B. Goedkoop, B.T. Thole, G. van der Laan, G.A. Sawatzky, F.M.F. de Groot, J.C. Fungle, Phys. Rev. B, **37**, 2086 (1988)

[51] F.M.F. de Groot, *X-ray absorption of transition metal oxides*, PhD. thesis, Nijmegen (1991)

[52] E. Arenholz, *Magnetic Dichroism in Photoemission from Lanthanide Matherials: Basic Concepts and Applications*, PhD thesis, Berlin (1996)

[53] C.T. Chen, F. Sette, Y. Ma, S. Modesti, Phys. Rev. B, **42**, 7262 (1990)

[54] D. Alders, *Epitaxial transition metal oxide films studied by high energy spectroscopy*, PhD. thesis, Groningen (1996)

[55] W.L Roth, Phys. Rev. **111**, 772 (1958)

[56] M. Gerloch, R.C. Slade, *Ligand-field Parameters*, Cambridge (1973)

[57] B.N. Figgis, *Introduction to ligand fields*, John Wiley & Sons, Inc (1966)

[58] C.J. Ballhausen, *Introduction to ligand field theory*, McGraw-Hill, New York (1962)

[59] M.W. Maurits, *Near-ground state symmetries and x-ray absorption spectra of transition metal thin films*, Master thesis, Groningen (2002)

[60] M.W. Haverkort, S.I. Csiszar, Z. Hu, S. Altieri, A. Tanaka, H.H. Hsieh, H.-J. Lin, C.T. Chen, T. Hibma and L.H. Tjeng, Phys. Rev. B, **69**, 020408(R) (2004)